



Modelling and measurements of gas tungsten arc welding in argon–helium mixtures with metal vapour

Junting Xiang^{1,2} · Keigo Tanaka³ · Fiona F. Chen¹ · Masaya Shigeta³ · Manabu Tanaka³ · Anthony B. Murphy⁴ 

Received: 6 October 2020 / Accepted: 18 December 2020 / Published online: 2 January 2021
© International Institute of Welding 2021

Abstract

Argon–helium mixtures in gas tungsten arc welding of an iron workpiece are investigated using an axisymmetric computational model that includes the cathode, workpiece, and arc plasma in the computational domain. The three-gas combined diffusion coefficient method is used to treat diffusion of helium, argon, and iron vapour. Calculations for argon–helium mixtures without metal vapour are performed; good agreement with previous numerical results is found. A transition from a helium-like to an argon-like arc occurs when the argon mole fraction increases above about 0.3. Calculations for a wide range of argon–helium mixtures including iron vapour are then performed. Adding helium to argon alters the arc properties and affects the weld geometry. Iron vapour cools the arc for all argon–helium mixtures. Iron vapour is present above the workpiece, near the cathode and in the arc fringes for very low argon mole fractions. As the argon mole fraction increases, the iron vapour becomes increasingly confined to the region above the workpiece, with small amounts near the cathode tip. Emission spectroscopy measurements of arcs in argon–helium mixtures with water-cooled copper and uncooled iron workpieces were performed. The measured distributions of atomic helium and iron emission show good agreement with the predictions of the model.

Keywords Gas tungsten arc welding · Argon–helium mixture · Demixing · Metal vapour · Computational modelling · Emission spectroscopy

1 Introduction

Gas tungsten arc (GTA) welding is widely used for welding metals [1, 2]. In GTA welding, an electric arc initiated between the tungsten cathode and anode workpiece generates high heat flux and melts the workpiece. The use of gas shielding is important in GTA welding to avoid contamination of welded areas and to enhance the weld quality. The choice of

shielding gas is critical in determining the arc plasma properties and weld quality. It has been shown that using shielding gas with high specific heat, thermal conductivity, and viscosity increases the weld pool depth [3]. Mixtures of shielding gases are commonly used in industry to achieve optimal performance and have proven to be effective [4, 5].

Extensive work has been performed to investigate the effect of different shielding gas on arc properties. Tanaka et al. [6] performed theoretical calculations to predict arc properties using a variety of pure shielding gases, including argon, helium, hydrogen, and nitrogen, respectively. Argon is often used as shielding gas due to its inertness and affordability. However, pure argon shielding is sometimes not effective because of the relatively low heat flux in an argon arc, resulting in a shallow weld pool. Significant efforts have been made to investigate the effect of mixed shielding gases on arc properties by adding other gases into argon, aiming to increase the heat flux. Lowke et al. [7] developed a theoretical model to assess the effect of adding hydrogen to argon for welding aluminium. Tusek [8] conducted experiments to examine the effect of adding hydrogen to argon for welding steel and aluminium. Marya et al. [9] compared experimental

Recommended for publication by Study Group 212 - The Physics of Welding

✉ Anthony B. Murphy
tony.murphy@csiro.au

- ¹ CSIRO Manufacturing, PO Box 10, Clayton South, VIC 3169, Australia
- ² Department of Mechanical Engineering, University of Melbourne, Melbourne, VIC 3010, Australia
- ³ Joining and Welding Research Institute, Osaka University, 11-1 Mihogaoka, Osaka, Ibaraki 567-0047, Japan
- ⁴ CSIRO Manufacturing, PO Box 218, Lindfield, NSW 2070, Australia

measurements of weld profiles between pure argon and mixtures of argon, helium, and nitrogen. Lu et al. [10] presented studies of adding oxygen to argon gas. Valiente Bermejo et al. [11] investigated the influence of shielding gases on welding performance and properties of duplex and super-duplex pipes using argon, helium, nitrogen, and carbon dioxide. Murphy performed calculations to determine the transport coefficients of argon and argon–helium mixtures [12]. Murphy also investigated the demixing of gases in a free-burning arc [4, 13] and discussed the properties of argon–helium arcs, argon–hydrogen arcs, and argon–nitrogen arcs [5]. Despite the advances of knowledge of the influence of shielding gas mixtures on arc properties, questions remain regarding the fundamental physics and optimised choice of shielding gas mixtures in GTA welding. Besides that, the effects of metal vapour on welding arcs have been extensively reported recently, demonstrating the influence of metal vapour on arc properties and weld quality both experimentally and theoretically [14–21]. For example, Wagner et al. [22] found that demixing of argon and helium during welding of stainless steel leads to a significant change of arc behaviour when metal vapour is included and when helium content is larger than 80%. The fundamental physics underlying this observation is, however, unknown. In particular, no model has included the influence of metal vapours together with the demixing of the shielding gases.

This work investigates the demixing of gas mixtures and the influence of metal vapour during GTA welding simultaneously, using a computational model including the tungsten cathode, workpiece anode, arc plasma, and weld pool. Argon–helium mixtures and iron vapour evaporated from the weld pool are considered. Other metal vapour species evaporated from steel welding are not included in this study, although their effects are also important [15, 17]. Iron is the largest component of stainless steel (79% by mass for SS 314) and other steels; an iron workpiece and iron vapour are used in this study as a reasonable representation of other metal species. The combined diffusion coefficient method, extended to three gases [23], is used in this study to treat the diffusion of each gas. The method calculates diffusion driving forces due to mole fraction gradients, temperature gradients, pressure gradients, and the applied electric field for each gas.

In this work, section 2 introduces the mathematical model and the boundary conditions. Section 3 presents three case studies, focusing on the model validation in section 3.1, argon–helium mixtures without metal vapour in section 3.2, and argon–helium mixture including metal vapour in section 3.3. Section 4 presents spectroscopic measurement results for argon–helium arcs with water-cooled copper and iron workpieces, allowing the influence of iron vapour to be measured and compared with predictions of the model. Section 5 concludes with the main findings from this study and discusses potential further work.

2 Methods

An axisymmetric computational model, including the tungsten cathode, workpiece anode, arc plasma, and weld pool, has been built to calculate the gas tungsten arc welding process [15]. The computational domain has dimensions of 31.6 mm × 43.0 mm, where 82 and 169 grid points are specified in the radial and axial directions, respectively. The cathode is defined with a full tip angle of 60 degrees and a diameter of 3.2 mm. The arc length can be chosen as either 5 mm or 3 mm for the different cases specified in section 3. Figure 1 shows the details of the axisymmetric computational domain, with 3-mm arc length for illustrative purpose. Shielding gas is applied from the top of the computational domain guided by a virtual nozzle with a diameter of $d_{nozz} = 14$ mm. Open boundary is applied for top and side walls, except the nozzle and workpiece region as pointed out in Fig. 1. Other boundary conditions are kept identical with our earlier calculations [15].

An in-house computational code has been developed to solve a set of governing equations including conservation equations of mass, momentum, and energy as well as the current continuity equation simultaneously. For iron in an argon–helium mixture, the governing equations are given as:

Conservation of mass:

$$\nabla \cdot (\rho \mathbf{v}) = S_{Fe} \quad (1)$$

where ρ is the mass density, \mathbf{v} is the plasma or liquid metal flow velocity, and S_{Fe} is the source term due to the production of iron vapour from the surface of the workpiece. Note that the metal vapour source term is only applied to the arc plasma domain in the region immediately above the weld pool. This also applies to Eq. (6).

Conservation of momentum:

$$\nabla \cdot (\rho \mathbf{v} \mathbf{v}) = -\nabla P + \nabla \cdot \tilde{\boldsymbol{\tau}} + \mathbf{j} \times \mathbf{B} + \rho \mathbf{g} \quad (2)$$

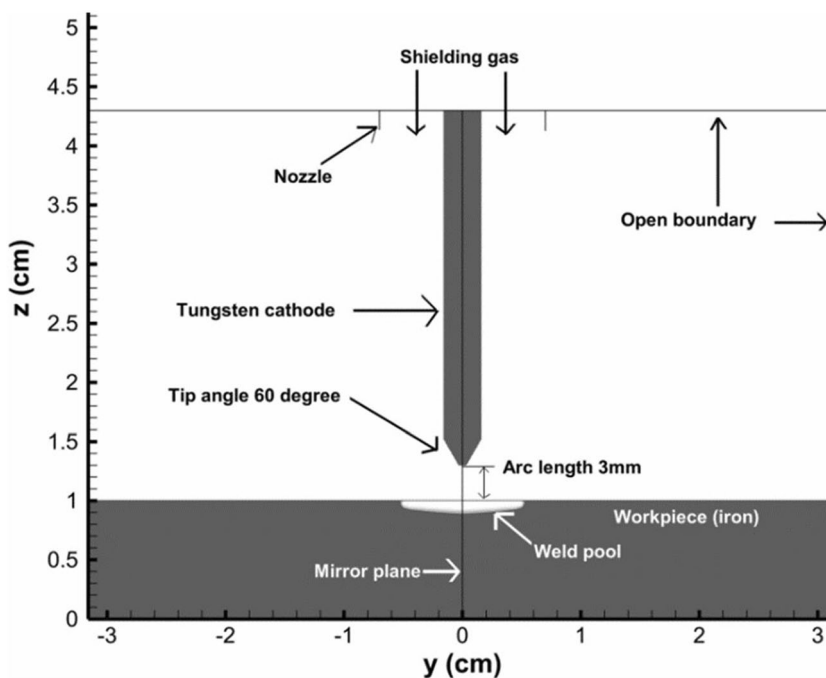
where P is the pressure, $\tilde{\boldsymbol{\tau}}$ is the viscous stress tensor, \mathbf{j} is the current density, \mathbf{B} is the magnetic field strength induced by the current, and \mathbf{g} is the gravitational acceleration.

Conservation of energy:

$$\begin{aligned} \nabla \cdot (\rho \mathbf{v} h) = & \frac{\mathbf{j}^2}{\sigma} - \nabla \cdot \left(\frac{k}{c_p} \nabla h \right) - \nabla \cdot \left[\left(\overline{h_{Fe}} - \overline{h_{Ar}} \right) \frac{k}{c_p} \nabla \overline{Y_{Fe}} \right] \\ & - \nabla \cdot \left[\left(\overline{h_{He}} - \overline{h_{Ar}} \right) \frac{k}{c_p} \nabla \overline{Y_{He}} \right] - \frac{5k_B}{2ec_p} \mathbf{j} \\ & \cdot \nabla h - U - S_{vap Fe} \end{aligned} \quad (3)$$

where h is the enthalpy, σ is the electrical conductivity, k is the thermal conductivity, c_p is the specific heat at constant pressure, $\overline{h_{Fe}}$ is the enthalpy of iron vapour, $\overline{h_{Ar}}$ is the enthalpy of argon, $\overline{h_{He}}$ is the enthalpy of helium, $\overline{Y_{Fe}}$ is the sum of mass

Fig. 1 Details of the axisymmetric computational domain



fraction of iron vapour species, $\overline{Y_{He}}$ is the sum of mass fraction of helium, e represents the electronic charge, k_B is the Boltzmann’s constant, U is the net emission coefficient, and $S_{vap Fe}$ is the latent heat of vaporisation of iron, which is applied only to the weld pool.

Current continuity equation:

$$\nabla \cdot (\sigma \nabla \phi) = 0 \tag{4}$$

where ϕ is the electric potential. The current density is expressed as:

$$\mathbf{j} = -\sigma \nabla \phi \tag{5}$$

The combined diffusion coefficient method has been used to successfully treat the mixing and demixing of plasma gases (e.g. [24–29]) under the local chemical equilibrium assumption. Metal vapour and a second shielding gas helium are included in the model, and additional mass conservation equations of metal vapour and helium are solved to maintain the mass balance. The respective conservation equations for iron vapour and helium are:

$$\nabla \cdot (\rho \mathbf{v} \overline{Y_{Fe}}) = -\nabla \cdot \overline{\mathbf{J}_{Fe}} + S_{Fe} \tag{6}$$

$$\nabla \cdot (\rho \mathbf{v} \overline{Y_{He}}) = -\nabla \cdot \overline{\mathbf{J}_{He}} \tag{7}$$

The diffusion mass flux terms $\overline{\mathbf{J}_{Fe}}$ and $\overline{\mathbf{J}_{He}}$ are respectively the average mass flux of the iron vapour and helium species, relative to the mass-average velocity. The mass flux term is determined by using the combined diffusion coefficient method [30], which treats gas diffusion due to mole fraction

gradients, temperature gradients, pressure gradients, and the electric field. The mass fraction of argon is calculated using $\overline{Y_{Fe}} + \overline{Y_{He}} + \overline{Y_{Ar}} = 1$ after solving Eqs. (6) and (7).

The expression for $\overline{\mathbf{J}_{Fe}}$ when calculating argon–helium mixtures including iron vapour is:

$$\overline{\mathbf{J}_{Fe}} = \frac{n^2}{\rho} \overline{m_{Fe}} \overline{m_{Ar}} \overline{m_{He}} \left[\left(\overline{D_{Fe Ar}^x} \nabla \overline{x_{Ar}} + \overline{D_{Fe He}^x} \nabla \overline{x_{He}} \right) + \overline{D_{Fe}^P} \nabla \ln P + \overline{D_{Fe}^E} \mathbf{E} \right] - \overline{D_{Fe}^T} \nabla \ln T \tag{8}$$

where n is the number density of the gas mixture; $\overline{m_{Fe}}$, $\overline{m_{Ar}}$, and $\overline{m_{He}}$ are the average masses of the heavy species of iron, argon, and helium gas, respectively; $\overline{x_{Ar}}$ and $\overline{x_{He}}$ are the sum of the mole fractions of species argon and helium respectively; $\overline{D_{Fe Ar}^x}$ and $\overline{D_{Fe He}^x}$ are the combined ordinary diffusion coefficients of iron relative to argon and helium respectively; and $\overline{D_{Fe}^P}$, $\overline{D_{Fe}^E}$, and $\overline{D_{Fe}^T}$ are the combined pressure diffusion coefficient, the combined electric field diffusion coefficient, and the combined temperature diffusion coefficient of iron, respectively. The expression for $\overline{\mathbf{J}_{He}}$ is analogous. Expressions for the combined diffusion coefficients are given in [23].

Equations (1) to (5) apply in the arc and electrodes. The viscosity is set to a very high value in the solid regions. The heat fluxes between the arc and the electrodes are treated using the methods presented by Lowke et al. [31, 32]. The heat flux to the anode is given by:

$$S = j_e \varnothing_w - k \partial T / \partial z \quad (9)$$

where j_e represents electron current density, assumed equal to the total current density, and \varnothing_w is the anode work function. Thermal conduction is taken into account through Eq. (3).

The thermodynamic and transport properties of argon–helium plasmas were calculated using the methods presented in [12], and those of iron vapour as described in [33]. Net emission coefficients were calculated using a mole fraction–weighted average of those for argon [34], helium [35], and iron [36]. Steady-state simulations are performed, and 50,000 iterations are typically required for the calculation to converge.

3 Results and discussion

Three sets of calculations were carried out in this work.

- (1) Model validation: Calculations for an argon (90% by mass) and helium (10% by mass) mixture without metal vapour were performed for a 5-mm arc length. The calculation results are validated by comparison with published numerical results.
- (2) Argon–helium mixture without metal vapour: Calculations for a wide range of argon–helium mixtures without metal vapour were performed for a 3-mm arc length. The calculation results are compared to assess the effect of demixing.
- (3) Argon–helium mixture with metal vapour: Calculations using the same conditions as case 2 but including iron vapour were carried out. The calculation results are compared with those of case 2 to understand the effect of metal vapour.

3.1 Model validation

The model has been validated previously for a pure helium arc including two metal vapours, with the predicted metal vapour distributions in the arc matching well with measurements [15]. In this section, we performed calculations for a GTA arc in an argon–helium mixture without metal vapour, to assess the reliability of the model in predicting demixing. The current model is an extension of a previous two-gas model [30, 37] to three gases [23]. To verify that the current model is able to predict gas mixing and demixing reliably, we apply the model to a mixture of two gases to reproduce published literature data [13]. An arc length of 5 mm, a gas mixture of 90% (by mass) argon and 10% (by mass) helium, 200-A arc current, and 10-L/min shielding gas flow are used, matching the

condition used in [13]. Other boundary conditions remain unchanged, as given in [15].

Figure 2 shows the isopleth maps of the mass fraction of helium calculated with the current model and the literature data, respectively. Note that helium mass fraction values labelled in Fig. 2(b) should be multiplied by 10 to give the true value [13]. The current model reproduces the isopleths of helium mass fraction reasonably well. Helium gas tends to concentrate near the arc axis and forms a bell-shaped distribution. This model predicts slightly more extended helium concentration near the anode surface, i.e. the high helium concentration extends to larger radii, though the overall helium isopleths in the arc are well reproduced. Note that this model calculation in Fig. 2(a) treats all diffusion coefficients described in section 2, whereas the published data in Fig. 2(b) include two sets of plots: results with all diffusion coefficients (the solid lines) and results neglecting electric field diffusion (the dashed lines).

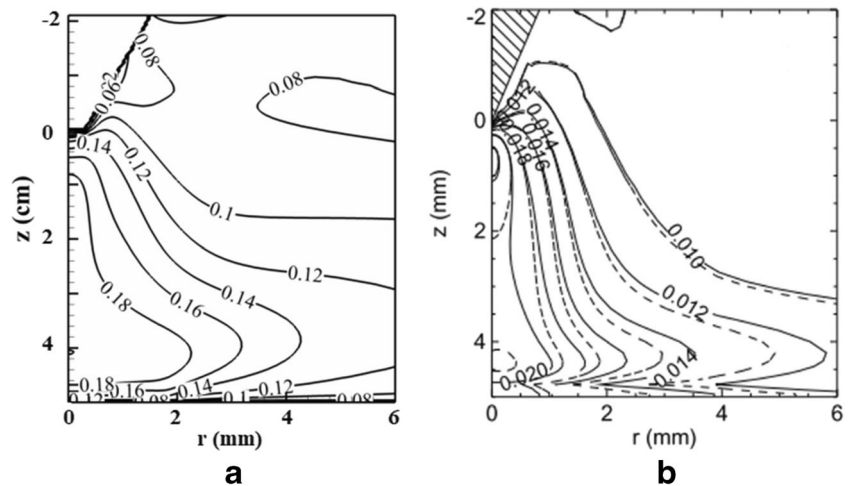
Figure 3 shows the isotherms calculated with this model and the literature data, respectively. The isotherms are closely reproduced by using this model. A slightly expanded 16,000-K contour is predicted near the anode by using the current model, showing a slight expansion of the high-temperature region. This corresponds to the expanded region of high helium concentration above the anode.

In general, the results match reasonably well with literature results. We do not expect exact agreement, particularly near the cathode, since in [13], the cathode surface temperature distribution was taken from measurements performed in an argon arc, whereas we have calculated the temperature self-consistently. The cathode surface temperature distribution influences the current density and therefore the arc temperature. The bell shapes of the isopleths of helium mass fraction and isotherm lines predicted from both models show good agreement. This demonstrates that the current model is capable of predicting the properties of a GTA arc in an argon–helium mixture and provides confidence that it can be relied upon to carry out the subsequent calculations.

3.2 Argon–helium mixture without metal vapour

Calculations with a range of argon–helium mixtures are performed in this section to assess the effect of demixing without metal vapour. Unlike section 3.1, an arc length of 3 mm, 150-A arc current, and 30-L/min gas flow are used hereafter to make them consistent with our earlier calculations [15, 16] for purposes of comparison. Six combinations of mole fractions of argon–helium gas mixtures, 0.01/0.99, 0.05/0.95, 0.1/0.9, 0.3/0.7, 0.5/0.5, and 0.7/0.3, and pure argon are tested. The percentage of mole fractions in the mixtures chosen here represents a more widely used quantity in real welding practice. Table 1 gives the conversion between the mole and mass fractions of argon

Fig. 2 Isoleths of the mass fraction of helium calculated for a 200-A, 5-mm arc with a 10-L/min input flow composed of 10% helium and 90% argon by mass **a** calculated by using the current model and **b** reproduced from literature data [13] (—) including and (---) neglecting the effects of electric field diffusion (cataphoresis); in **b**, mass fraction values need to be multiplied by a factor of 10 to give the correct value. © IOP Publishing. Reproduced with permission. All rights reserved



and helium used in this study. Values are calculated at atmospheric pressure and a temperature of 300 K.

It has been shown that mixing helium with argon affects critical shielding gas properties, including specific heat, electrical conductivity, thermal conductivity, and viscosity. Figure 4 shows the dependence of these properties on temperature for argon–helium mixtures and pure argon at 1 atm. It has been pointed out that the small electrical conductivity for helium leads to a constricted arc, resulting in increased heat flux density on axis compared to an argon arc. Detailed discussions about the gas property changes in argon–helium mixtures were presented in [5]. In this section, we focus on the effect of argon–helium mixture on arc properties and on the welding quality.

Figure 5 shows the temperature distribution in argon–helium GTA arcs with argon mole fractions of 0.01, 0.1, 0.3, and 0.5. The arc shape remains largely unchanged when the argon mole fraction increases, although a gradual decrease of arc temperature is

predicted when the argon mole fraction increases from 0.01 to 0.3. Increasing the argon mole fraction from 0.01 to 0.3 reduces the maximum arc temperature from 21,800 to 19,200 K. Further increase of argon mole fraction has little influence on arc temperature. This is in accordance with the results of Murphy et al. [5], who showed that adding up to 70% helium (by mole) to argon has little influence on arc temperature and the temperature distribution resembles that of a pure argon arc. This will be confirmed by the spectroscopic measurements presented in section 4.

Figure 6 shows the demixing of argon and helium gases. Argon tends to be distributed away from the arc centre, indicating the concentration of helium near the arc axis. It was noted in [24] that demixing due to mole fraction gradients, frictional forces, and thermal diffusion all act in the same direction by driving diffusion of helium species, i.e. the chemical element with lower atomic weight and higher ionisation energy, to regions with higher temperature.

Fig. 3 Isotherms calculated for a 200-A, 5-mm arc with a 10-L/min input flow composed of 10% helium and 90% argon by mass **a** calculated by using the current model (labelled in units of K) and **b** reproduced from [13] (labelled in units of 1000 K). © IOP Publishing. Reproduced with permission. All rights reserved

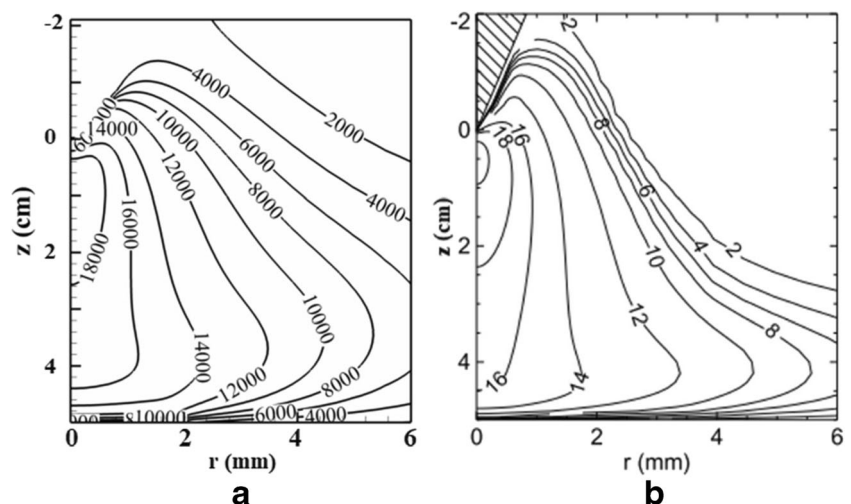


Table 1 Argon–helium mixtures used in this work

Pressure	Temperature	Argon atomic weight	Helium atomic weight	Argon mole fraction	Helium mole fraction	Argon mass fraction	Helium mass fraction
1 atm	300 K	39.948	4.0026	0.01	0.99	0.0916	0.9084
				0.05	0.95	0.3444	0.6556
				0.1	0.9	0.5258	0.4742
				0.3	0.7	0.8105	0.1895
				0.5	0.5	0.9089	0.0911
				0.7	0.3	0.9588	0.0412
				1.0	0.0	1.0	0.0

It is known that the heat flux to the workpiece is much higher in a helium arc than an argon arc, resulting in a deeper weld pool. This is a consequence of the higher temperature and stronger constriction of

the helium arc. Furthermore, calculations performed without accounting for demixing show that the heat flux increases with the helium concentration in an argon–helium arc [5]. The concentration of helium near the

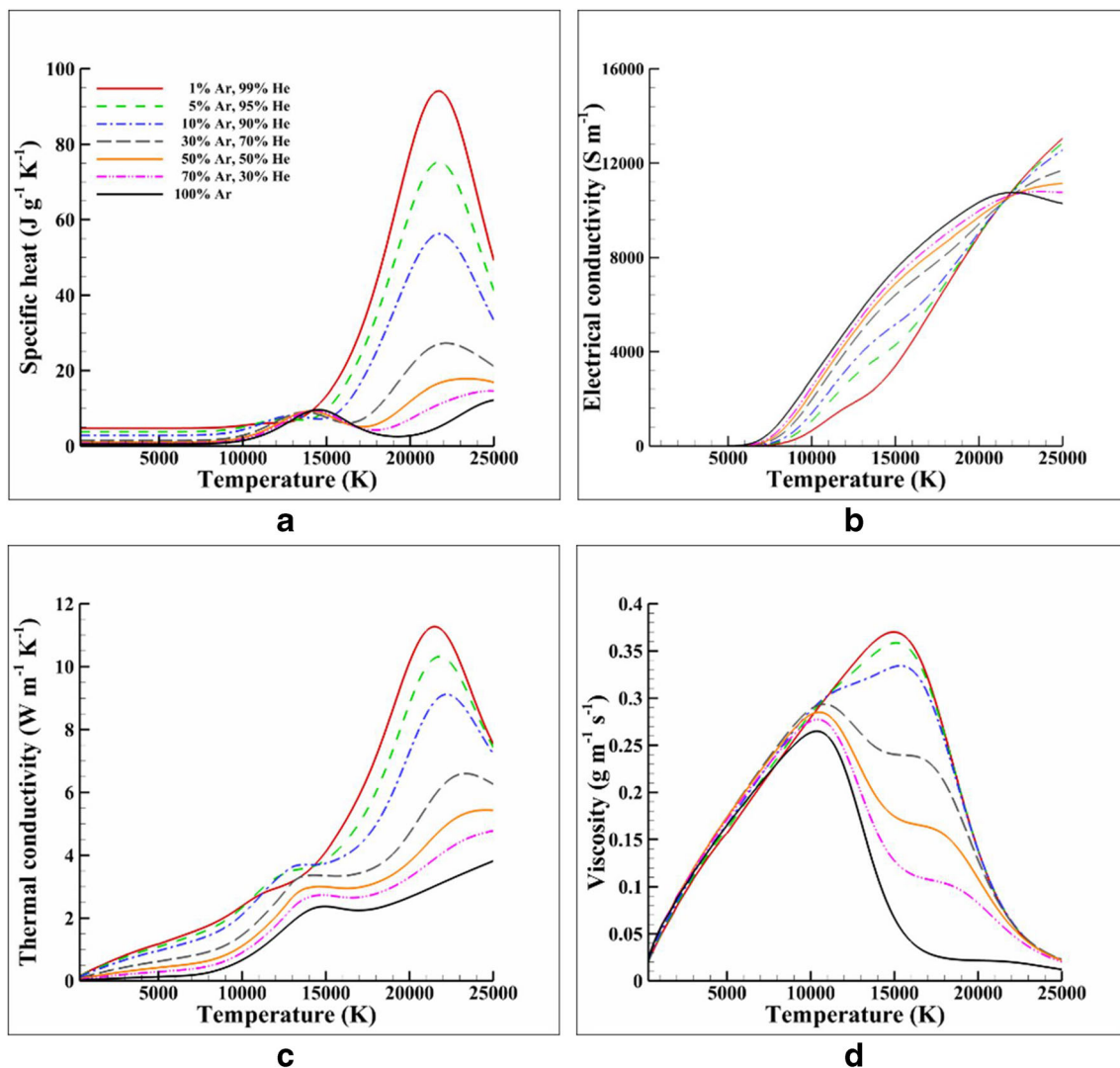


Fig. 4 Dependence of **a** specific heat, **b** electrical conductivity, **c** thermal conductivity, and **d** viscosity on temperature for argon–helium mixtures and pure argon at 1 atm. Percentages are mole percentages

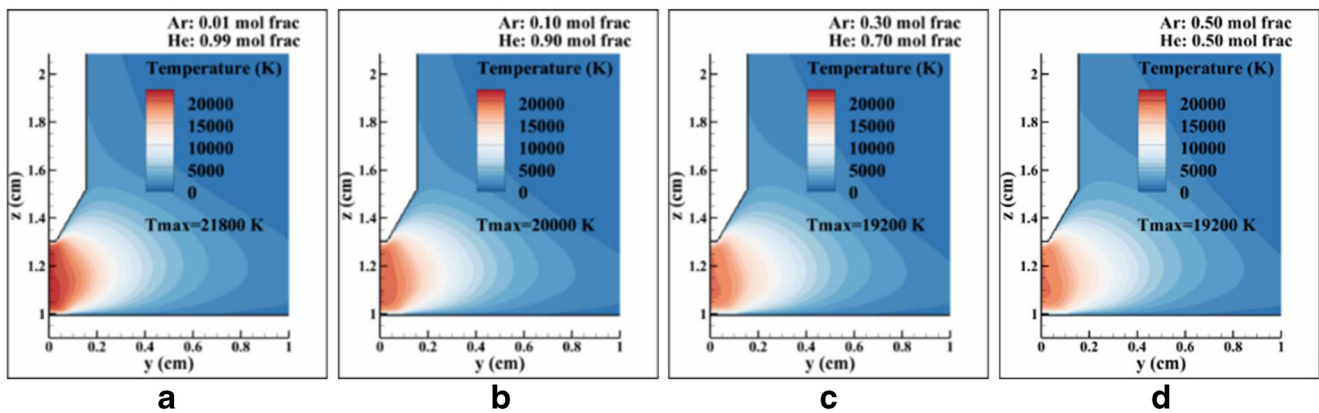


Fig. 5 Distribution of temperature in a GTA arc for argon mole fractions of **a** 0.01, **b** 0.1, **c** 0.3, and **d** 0.5

arc centre due to demixing increases this effect and results in a deeper weld pool.

Figure 7 shows the net emission coefficient distribution for different argon–helium mixtures. For argon mole fractions less than 0.3, the arc is constricted and resembles a helium-dominated arc. For argon mole fractions of 0.3 and greater, the arc is more radially extended and resembles an argon-dominated arc. The net emission coefficient distribution shows that radiative emission in the arc centre is stronger in a helium-dominated arc than that in an argon-dominated arc. This is because the temperature is the highest in the helium-dominated arc. The net emission coefficient of argon is about a factor of seven larger than that of helium at 20,000 K [35]. However, in all cases, the argon mole fraction is low in the centre of the arc, so the increase in net emission coefficient with temperature is the dominant factor. Away from the arc centre, the net emission coefficient of the argon-dominated arc is higher. This is because argon mole fraction is higher in this region, and the higher net emission coefficient of argon dominates.

3.3 Argon–helium mixture with iron vapour

Calculations with a range of argon–helium mixtures taking into account the presence of iron vapour were performed to

study the combined influence of metal vapour and gas demixing. The presence of metal vapour in a pure helium arc has been demonstrated to strongly influence the radiative cooling of the arc [15]. The presence of metal vapour in a pure argon arc has been recently found to affect arc properties as well as the weld pool [38], even though it was expected that the effect of metal vapour would be small in an argon arc [39]. Since substantial demixing occurs in an argon–helium arc, it is important to consider the effect of demixing and metal vapour together for a better understanding of the influence of metal vapour on argon–helium arcs and of the underlying physics.

To examine the influence of metal vapour on plasma properties in an argon–helium mixture, a fixed argon–helium mixture (10% argon, 90% helium by mole) is used. Iron vapour mole fractions of 1%, 5%, 10%, and 20% are applied to the argon–helium mixture respectively, resulting in correspondingly updated values of argon and helium in the mixture due to mass balance in a computational cell ($\overline{Y}_{Fe} + \overline{Y}_{Ar} + \overline{Y}_{He} = 1$). For example, when 10% iron vapour mole fraction is used, the corresponding mole fraction of argon is 9% and helium is 81%, i.e. 90% of their predefined values. Figure 8 shows the distribution of gas properties for an argon–helium mixture including iron vapour at a pressure of 1 atm.

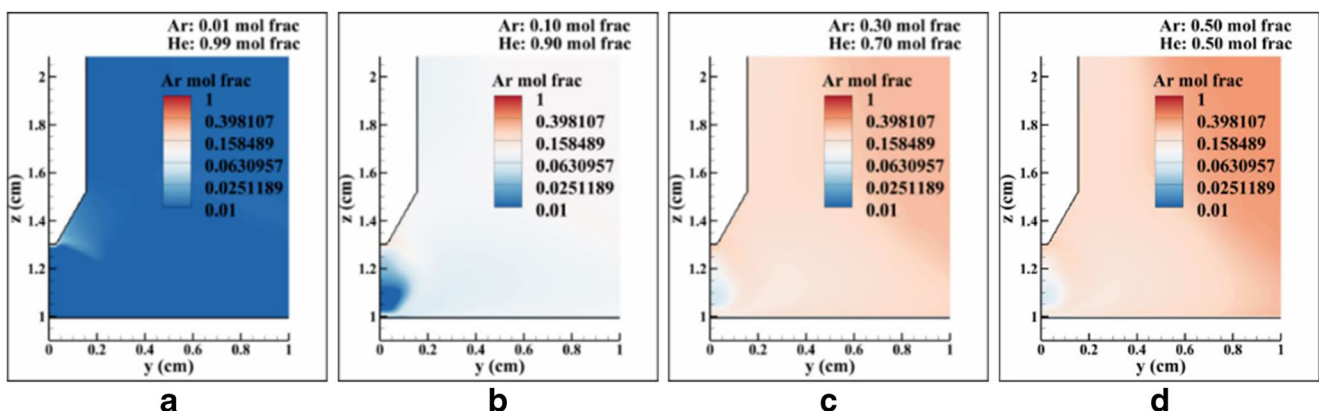


Fig. 6 Distribution of argon mole fraction in a GTA arc for argon mole fractions of **a** 0.01, **b** 0.1, **c** 0.3, and **d** 0.5

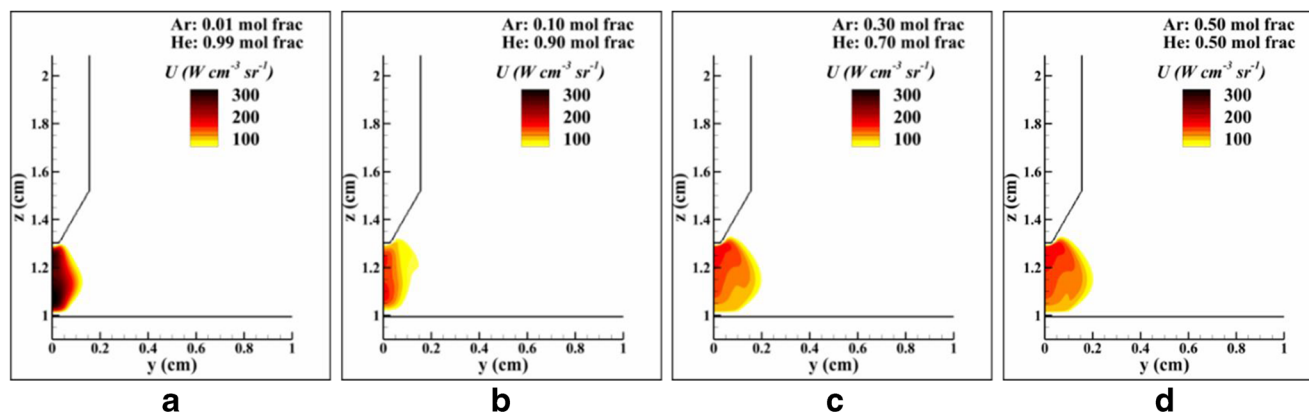


Fig. 7 Distribution of net emission coefficient in a GTA arc for argon mole fractions of **a** 0.01, **b** 0.1, **c** 0.3, and **d** 0.5

Figure 8(a) shows the dependence of specific heat on temperature for the different mixtures. Similar to those shown in Fig. 4(a) where specific heat is affected by the argon–helium ratio, specific heat is also strongly influenced by the concentration of iron vapour. With the increase of iron vapour mole fraction from 0.01 to 0.20, the peak specific heat (which occurs at a temperature of about 22,000 K) decreases by more than a half. Similar trends are apparent in the thermal conductivity, shown in Fig. 8(c). Both the specific heat and thermal conductivity appear in Eq. (3) for energy conservation, and so it is clear that the presence of metal vapour directly affects energy transport in the arc.

Figure 8(b) shows the dependence of electrical conductivity on temperature. In the temperature range from 5000 to 15,000 K, the electrical conductivity increases with the increase of iron vapour concentration. It was explained in [38] that iron atoms ionise at a lower temperature than argon, so the electron density and therefore the electrical conductivity are higher at low temperatures. At high temperature, the iron vapour has a higher degree of ionisation than argon, leading to a stronger Coulomb potential and therefore, since the transport coefficients are inversely proportional to the collision cross-sections, a lower electrical conductivity. This also applies when helium is included, as helium has an even higher ionisation temperature than argon.

Figure 8(d) shows the dependence of viscosity on temperature. The inclusion of iron vapour reduces the viscosity in the temperature range from 7000 to 18,000 K, affecting the momentum transfer in the arc. It was noted in [3] that high specific heat, thermal conductivity, and viscosity increase the weld pool depth. With the reduction in the values of these properties when iron vapour is present, a shallower weld pool depth is expected.

Figure 8(e) shows the dependence of the net emission coefficient on temperature. It shows that in an argon–helium mixture, the inclusion of iron vapour significantly increases the net emission coefficient. In the temperature range of

10,000 to 20,000 K for a typical arc, the inclusion of 5% iron vapour can amplify the radiative loss by around ten times. It has been shown that the increased radiation due to the presence of metal vapour can cool down arcs in pure helium [15] and in pure argon [38]. For an argon–helium arc, the influence of metal vapour on radiative cooling will also be significant.

To examine the effect of metal vapour in an argon–helium mixture shielded arc, similar parameters to those used in section 3.2 were chosen. An iron workpiece is used, with iron vapour evaporation from the weld pool calculated as presented in [38]. Iron vapour transport and diffusion in the arc are calculated using the combined diffusion coefficient method [30]. Unlike the calculations in sections 3.1 and 3.2, this calculation considers three gases in the arc, i.e. iron vapour, argon, and helium. The iron vapour mass flux \overline{J}_{Fe} is calculated using Eq. (8).

Figure 9 shows the temperature distribution for 0.01, 0.1, 0.3, and 0.5 argon mole fractions and including metal vapour. Comparing the arc shapes to those in Fig. 5, the region of relatively high temperature is not limited to radii < 0.05 cm when metal vapour is included. A significant drop of arc temperature is predicted when metal vapour is included regardless of the argon–helium mixture used, showing the strong influence of metal vapour on arc properties. Previous studies have shown that the presence of metal vapour leads to increased radiative cooling, reducing the arc temperature [15].

Figure 10 shows the distribution of iron vapour in the arc for the different argon–helium mixtures. To better understand the metal vapour distribution, results for a wider range of argon mole fractions are presented. Iron vapour is observed above the weld pool, near the cathode tip and in the arc fringes. Increasing the argon mole fraction is found to reduce the presence of iron vapour in the arc fringes. Figure 10(d) shows that nearly no iron vapour is predicted near the cathode tip and in the arc fringes for an argon mole fraction of 0.3. As noted in section 3.2, when the argon mole fraction increases to 0.3, the arc resembles

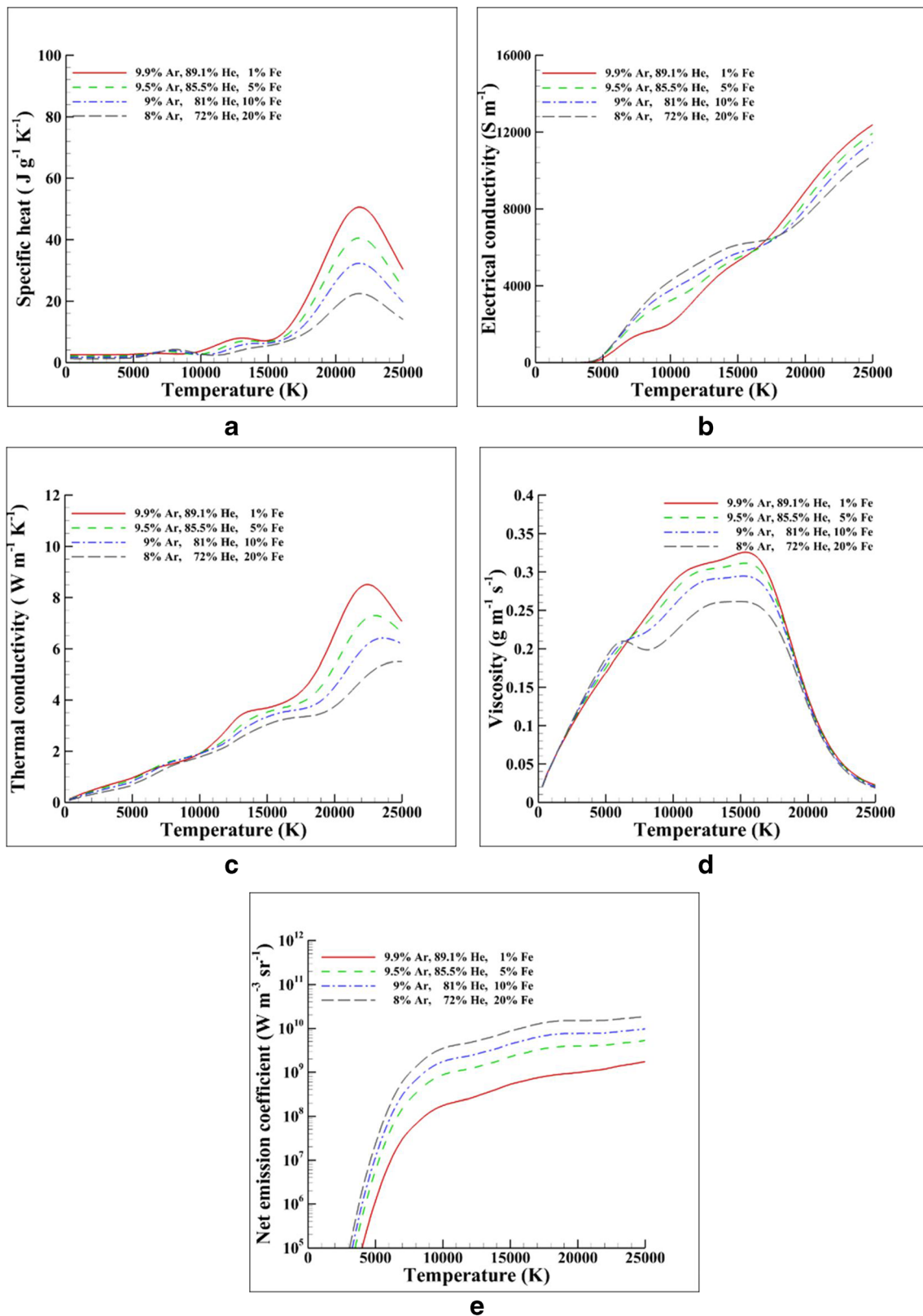


Fig. 8 Dependence of **a** specific heat, **b** electrical conductivity, **c** thermal conductivity, **d** viscosity, and **e** net emission coefficient on temperature for 1:9 argon–helium mixtures with iron vapour at 1 atm. Percentages are mole percentages

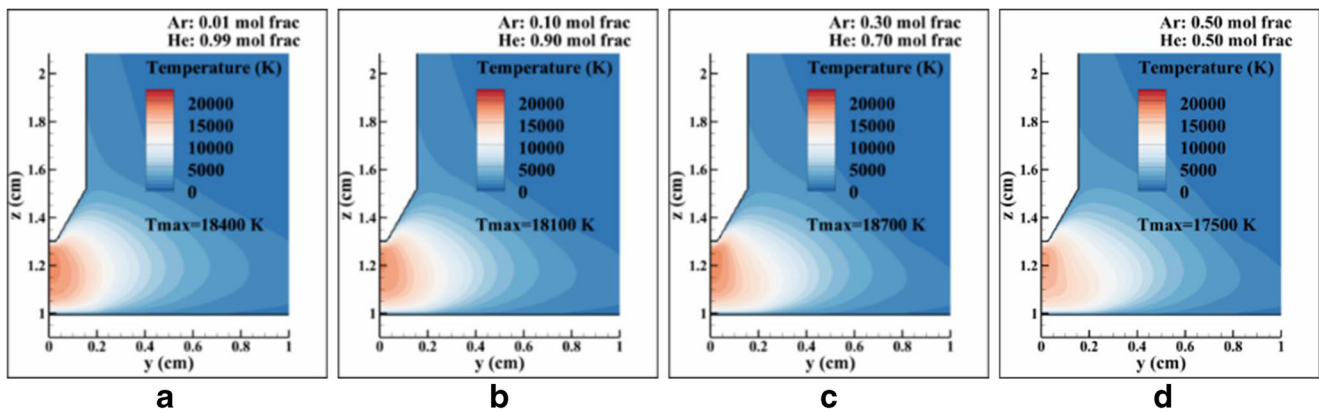


Fig. 9 Distribution of temperature in a GTA arc with metal vapour for argon mole fractions of **a** 0.01, **b** 0.1, **c** 0.3, and **d** 0.5

a pure argon arc. Furthermore, the heat flux to the workpiece approaches that of an argon arc as the argon mole fraction increases beyond 0.3 [5]. Nevertheless, Fig. 10 e and f show that iron vapour transport to the cathode tip

region in an argon-dominated arc is predicted with further increases of argon mole fraction above 0.3.

For a helium arc, it has been shown that the electric field diffusion, also known as cataphoresis, drives metal vapour

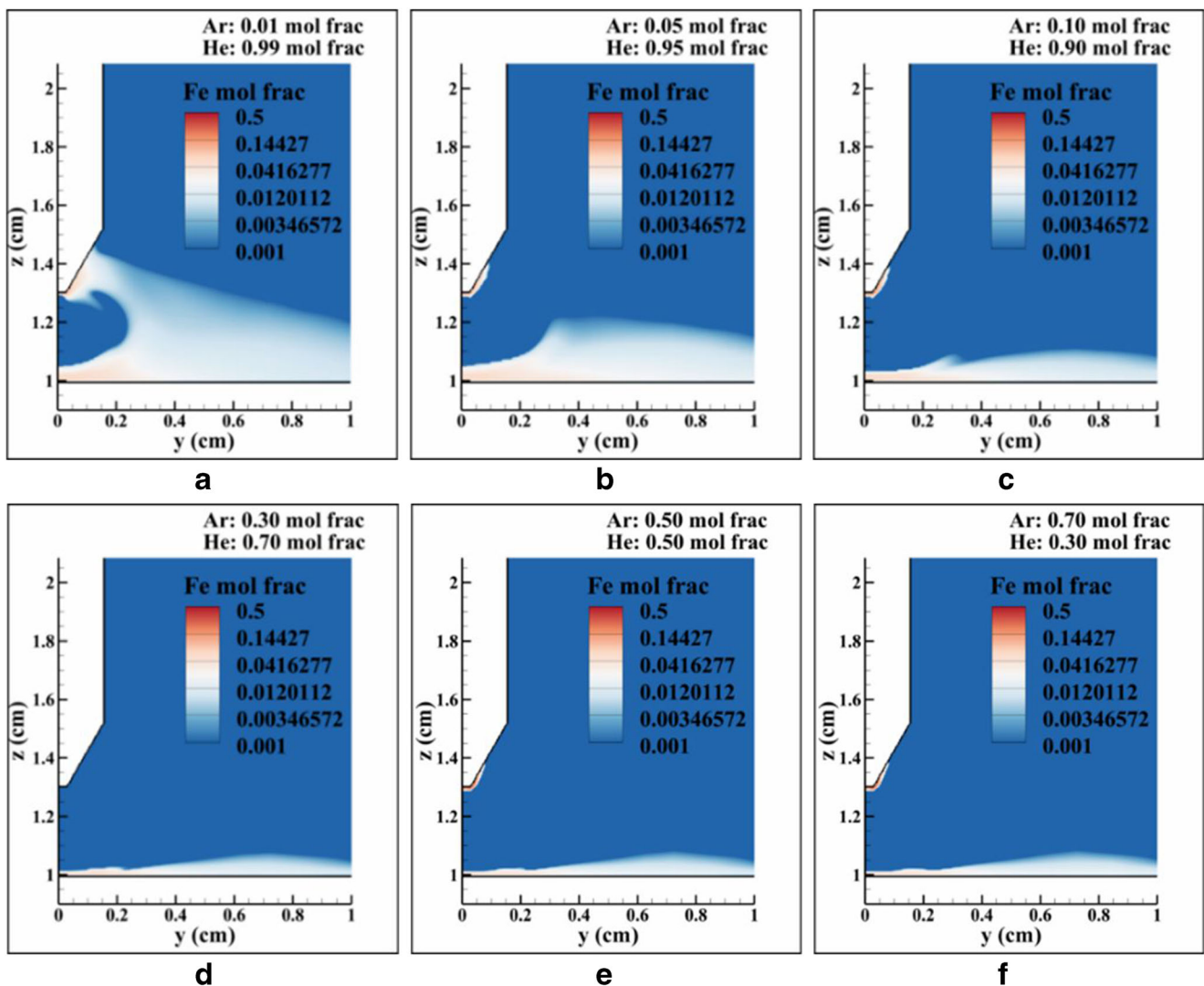


Fig. 10 Distribution of iron vapour in a GTA arc with metal vapour for argon mole fractions of **a** 0.01, **b** 0.05, **c** 0.1, **d** 0.3, **e** 0.5, and **f** 0.7

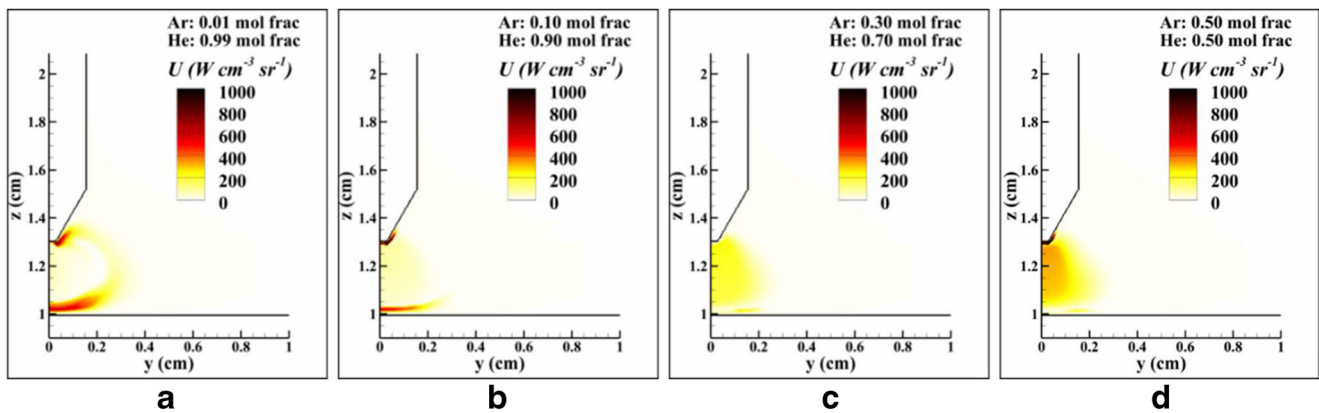


Fig. 11 Distribution of net emission coefficient in a GTA arc with metal vapour for argon mole fractions of a 0.01, b 0.1, c 0.3, and d 0.5

upwards through the arc [15]. For an argon arc, it was found that cataphoresis was not strong enough to overcome the downward convective flow and that the metal vapour near the anode is swept radially outwards. However, some metal vapour was then convected upwards in the recirculating flow and became trapped near the cathode tip by upward diffusion driven by temperature gradients and the electric field [38]. In the transition argon–helium ratio region (argon mole fraction of 0.3), neither of the mechanisms that occur in pure argon and helium is effective, and there is essentially no metal vapour transported upward through the arc, as shown in Fig. 10(d).

Figure 11 shows the net emission coefficient distributions in the arc for different argon–helium mixtures with metal vapour included. Strong radiative emission is predicted above the weld pool as well as near the cathode tip for argon mole fractions of 0.01 and 0.1. The net emission coefficient value is significantly higher than those predicted in Fig. 7, reflecting the intense radiation from iron vapour. For an argon mole

fraction of 0.3, the net emission coefficient distribution is significantly different, due to the change from a helium-like arc to an argon-like arc [5]. Further increase of argon mole fraction above 0.3 leads to increased net emission coefficient near the cathode tip, due to the presence of iron vapour.

Wagner et al. [22] presented measurements of argon–helium welding of mild steel or stainless steel. They measured large ultraviolet radiation intensities and ozone concentrations for argon mole fractions of 0 and 0.1, which fell rapidly to very low values at an argon mole fraction of 0.2, and then increased gradually as the argon mole fraction was increased further. These trends are in accordance with the net emission coefficients shown in Fig. 11. More extensive comparisons with experiment will be presented in section 4.

Figure 12 shows the radial distributions of current density above the weld pool with (the dashed lines) and without (the solid lines) iron vapour. When metal vapour is included, the current density near the arc axis is greatly reduced and has little dependence on the argon–helium ratio. The current density extends to a radius of 0.25 cm when metal vapour is present. When metal vapour is not included, the current is restricted to radii of less than 0.15 cm, and the peak value of current density decreases with increasing argon mole fraction for argon mole fractions less than 0.3. When metal vapour is present, current density distribution is dominated by the effects of metal vapour, regardless of the argon–helium ratio.

Figure 13 shows the weld pool shape for different argon–helium mixtures, neglecting and including iron vapour. When metal vapour is neglected, increasing the argon mole fraction results in a decrease of weld pool depth. The weld pool depth decreases from 0.9 to 0.7 cm when the argon mole fraction increases from 0.01 to 0.5. This is consistent with the decrease of current density within radii of 0.1 cm when the argon mole fraction increases, shown in Fig. 12, which leads to a reduced heat flux to the workpiece. When metal vapour is included, shallower weld pools are predicted. The weld pool depth decreases from 0.3 to 0.15 cm when the argon mole fraction increases from 0.01 to 0.5. Weld pool widths increase when metal vapour is included, consistent with the radially extended

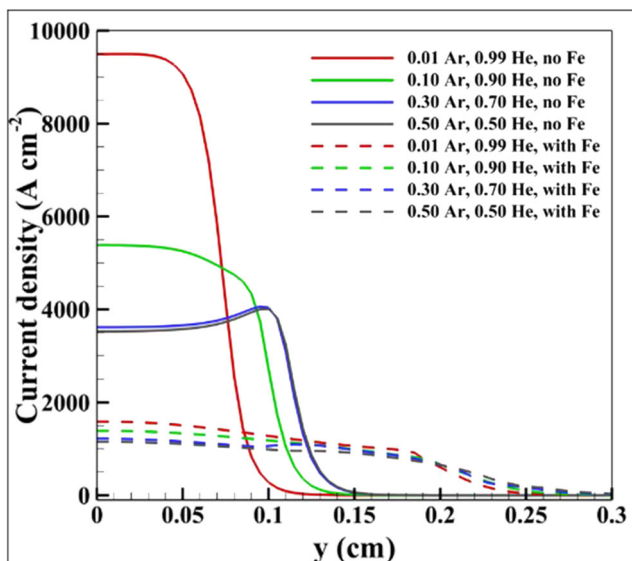


Fig. 12 Radial distribution of current density above the weld pool for argon mole fractions of 0.01, 0.05, 0.1, and 0.3, with and without iron vapour

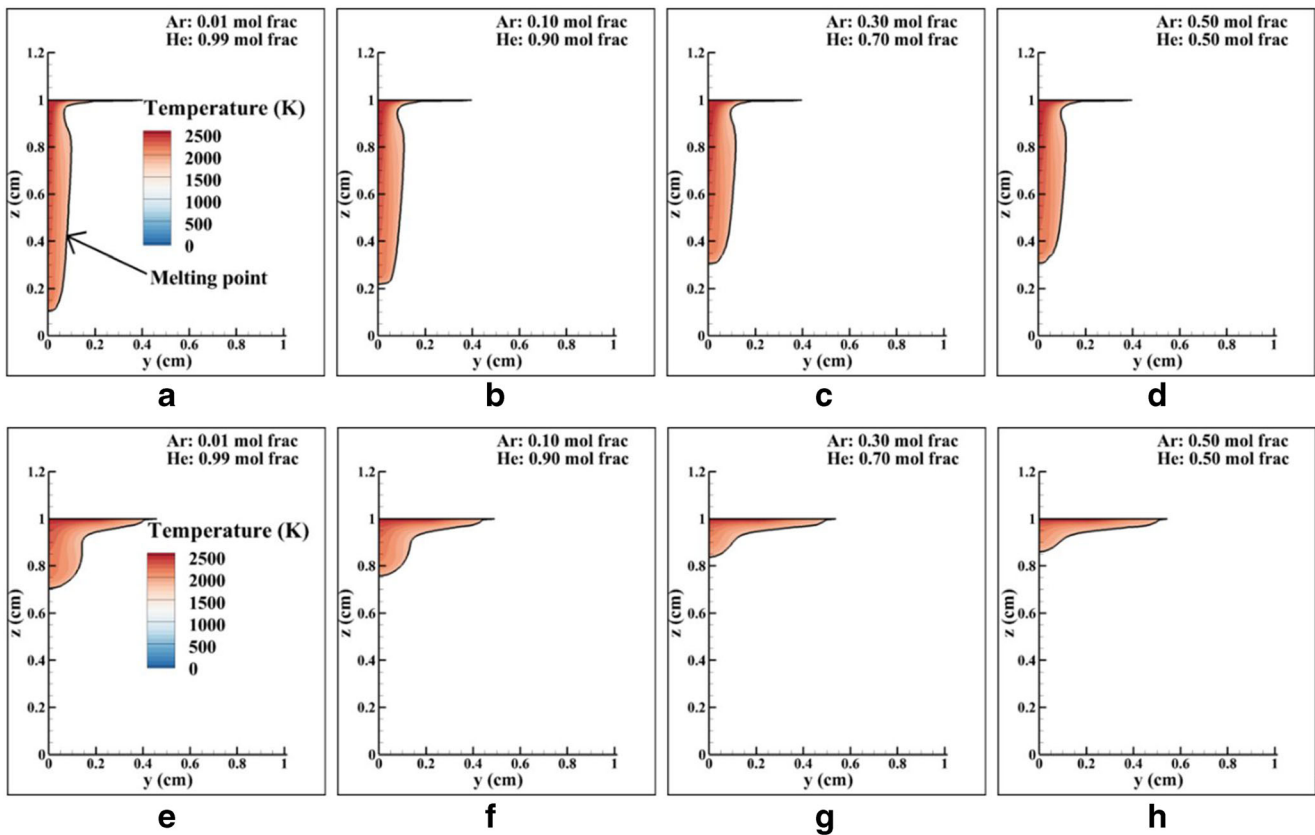


Fig. 13 Shape of weld pool when neglecting metal vapour for argon mole fractions of **a** 0.01, **b** 0.1, **c** 0.3, and **d** 0.5 and when including metal vapour for argon mole fractions of **e** 0.01, **f** 0.1, **g** 0.3, and **h** 0.5

distribution of current density shown in Fig. 12. Flow in the weld pool is driven by four main forces: the Lorentz ($j \times B$) force, buoyancy, the Marangoni force, and the drag force of the plasma on the weld pool surface. The latter three usually lead to liquid flows directed upward near the axis and outward near the surface, while the Lorentz force drives flow downwards near the weld pool axis [38].

In summary, when demixing and metal vapour are both considered, the arc properties are mainly influenced by the metal vapour, regardless of the argon–helium mixture used. The presence of metal vapour significantly changes the critical arc plasma properties such as arc temperature, current density, and net emission coefficient, and affects the weld pool depth and width. The argon–helium ratio strongly influences the upward transport of metal vapour, with the importance of the different transport mechanisms altered depending on whether argon [38], helium [15], or argon–helium mixtures are used.

4 Spectroscopic measurements

Measurements of Fe I and He I emission during stationary GTA welding under argon–helium mixture shielding were performed. Water-cooled copper and uncooled iron

workpieces were used, corresponding respectively to the cases in which iron vapour is neglected and included. The cathode is made of tungsten doped with 2% La_2O_3 . Emission spectroscopy analysis was performed using an Abel inversion to show the distribution of the metal vapours in the arc. Details of the experimental and image-processing methods have been given elsewhere [17, 40]. To obtain the argon–helium mixtures described in Table 1, a total gas flow rate of 20 L/min is applied and a gas mixer MX-4S (Yukata Engineering Corporation) is used with a flow metre range of 1–25 L/min for each gas and flow metre accuracy of 0.1 L/min.

Figure 14 shows the arc appearance for different argon–helium mixtures 20 s after ignition for the water-cooled copper workpiece. Figure 14(a) shows an expanded bell-shaped red arc when pure helium is used. When argon is added, the arc shape and appearance change. Figure 14 b and c show that when an argon mole fraction of 0.05 to 0.1 is added, the arc becomes constricted, the red region is confined to the lower half of the arc, and a purple region appears near the cathode tip, and in the case of an argon mole fraction of 0.1, the arc fringes. This is consistent with predictions in Fig. 6 a and b, which show that the argon tends to become concentrated in the vicinity of cathode tip and also the arc fringe regions for an argon model fraction of 0.1. Figure 14(d) shows that when argon mole fraction reaches 0.2, a bell-shaped light-purple

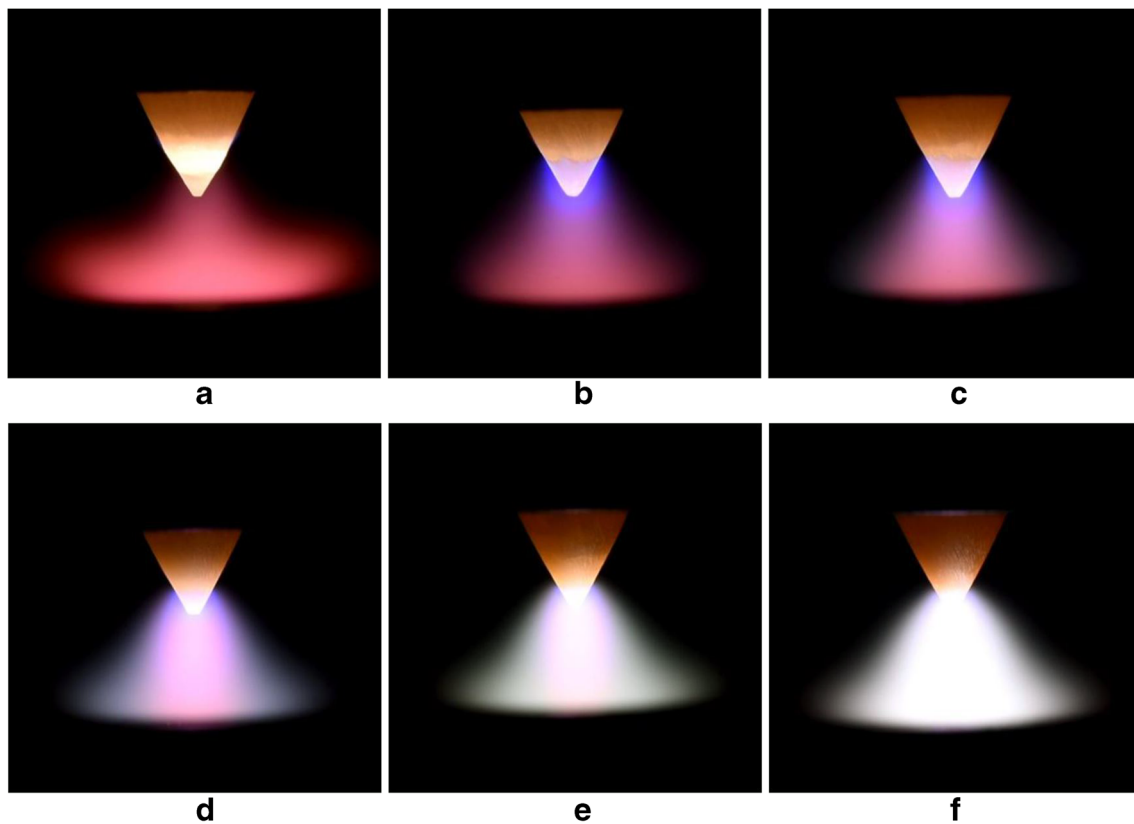


Fig. 14 Arc appearance for water-cooled copper workpiece 20 s after arc ignition for argon–helium ratios of **a** 0.0/1.0, **b** 0.05/0.95, **c** 0.1/0.9, **d** 0.2/0.8, **e** 0.3/0.7, and **f** 0.5/0.5

arc forms with a pink region observed near the arc axis. This demonstrates that helium tends to concentrate near the arc axis, as predicted by using our model. Figure 14(e) shows that when argon mole fraction reaches 0.3, a bell-shaped bright white arc appears, similar to a pure argon arc, with only a faint pink region near the arc axis. The strong radiation from argon diminishes the observability of helium, consistent with the prediction in Fig. 6(c). The measured He I spectral intensity distribution given in Fig. 15 confirms this phenomenon, showing concentrated helium near the arc centre.

Figure 15(a) corresponds to the calculation result shown in Fig. 7(b) for argon mole fraction of 0.1. Figure 15(c) corresponds to the calculation result given in Fig. 7(c) for argon mole fraction of 0.3.

The spectroscopic measurements for a water-cooled copper workpiece confirm the numerical prediction results given in section 3.2. An arc transition region exists near an argon–helium ratio of 0.3/0.7. When the argon mole fraction is larger than 0.3, an argon-like arc forms, with helium only visible near the arc centre. When the argon mole fraction is less than

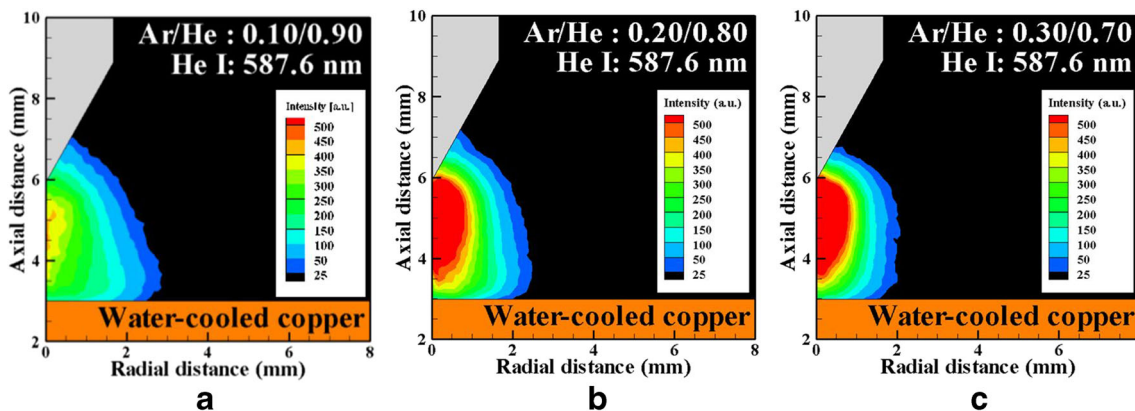


Fig. 15 He I spectral intensity distribution for water-cooled copper workpiece 20 s after arc ignition for argon–helium ratio of **a** 0.1/0.9, **b** 0.2/0.8, and **c** 0.3/0.7

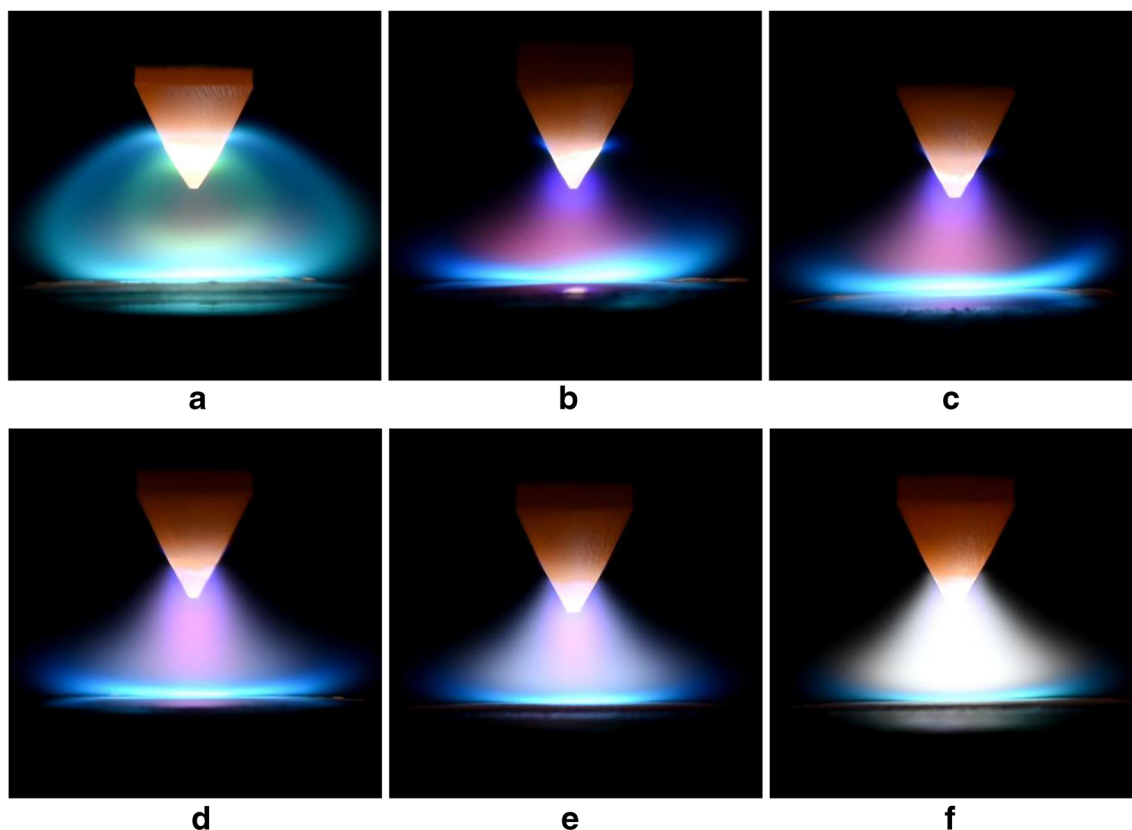


Fig. 16 Arc appearance in stationary GTA welding of pure iron workpiece 20 s after arc ignition for argon–helium ratios of **a** 0.0/1.0, **b** 0.05/0.95, **c** 0.1/0.9, **d** 0.2/0.8, **e** 0.3/0.7, and **f** 0.5/0.5

0.3, a transition from an argon-like to helium-like arc occurs, with helium visible at larger radii and argon expelled to regions in the vicinity of cathode tip and the arc fringes (Fig. 14b, c), until a complete helium arc is formed (Fig. 14a).

Figure 16 shows the arc appearance during stationary GTA welding of pure iron, 20 s after arc ignition. Unlike the results shown in Fig. 14, when an iron workpiece is used, evaporation of metal vapour occurs. Figure 16(a) shows the arc appearance for pure helium shielding. The bright blue regions show the presence of iron vapour above the weld pool and in the vicinity of cathode tip. In addition, a bilayer region of metal vapour exists as detailed in [17]. When argon is added to helium, the arc appearance changes dramatically. Figure 16(b) shows that when 0.05 mole fraction of argon is added, the metal vapour, indicated by the bright blue glow, is only visible above the weld pool and near the cathode tip. When the argon mole fraction is further increased, metal vapour above the weld pool remains while those near the cathode tip become less observable due to strong radiation of argon. Away from the electrodes, the arc region resembles those observed in Fig. 14.

Figure 17 shows the Fe I spectral intensity during stationary GTA welding of pure iron. Note that in the highest temperature regions, such as below the cathode tip, iron vapour will be ionised and therefore will not be detected. Atomic iron vapour is observed above the weld pool, near the cathode tip and in the

arc fringe region in Fig. 17(a) for the pure helium case. This is consistent with the prediction shown in Fig. 10(a), for which only 0.01 argon mole fraction is added, and which resembles a helium-like arc. When 0.05 mole fraction of argon is added to helium, shown in Fig. 17(b), iron vapour disappears from the arc fringe region and is only observed above the weld pool and near the cathode tip, again in accordance with the prediction of the model shown in Fig. 10(b). Increasing the argon mole fraction to 0.10 (Fig. 17c) reduces the axial extent of the iron vapour above the weld pool, as also predicted in Fig. 10(c).

When the argon mole fraction increases to 0.3 or more, an argon-like arc forms. Iron vapour is still present above the weld pool, while the amount of iron vapour near the cathode tip diminishes. As discussed in section 3.3, changing the argon–helium ratio affects the arc properties and therefore the metal vapour transport mechanism. In a helium arc, diffusion driven by the electric field dominates the upward transport of metal vapour [15]. In an argon arc, convection in the recirculating flow drives the metal vapour transport toward the cathode tip [16]. Note that only very low concentrations are predicted to occur in the recirculation zone in the arc fringes, with the iron vapour becoming trapped in the low flow regions immediately adjacent to the cathode by upward diffusion. Therefore, we do not expect to observe metal vapour in the fringe regions for an argon-like arc [38]. In general, the

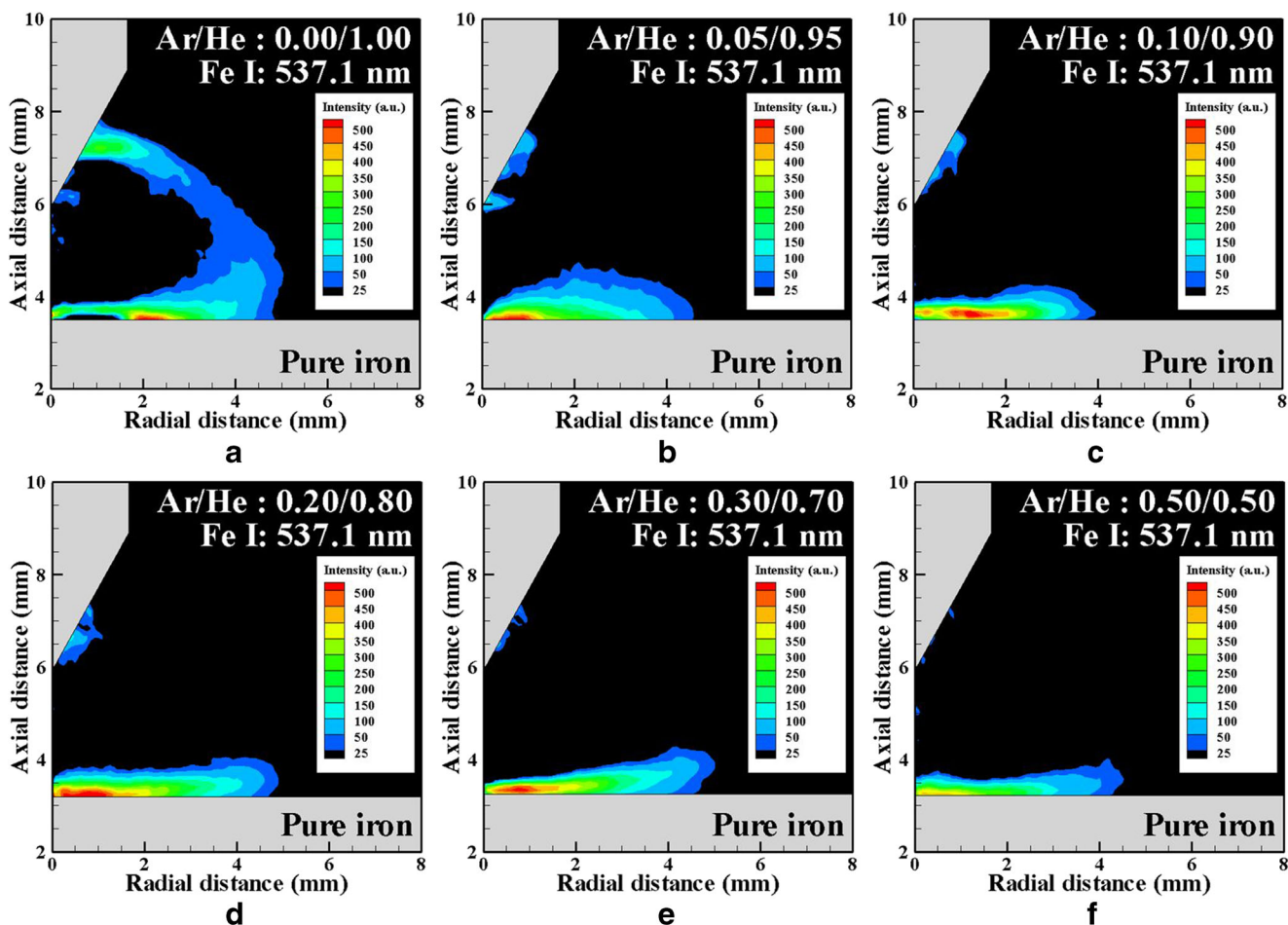


Fig. 17 Distribution of Fe I spectral intensity in stationary GTA welding of pure iron workpiece 20 s after arc ignition for argon–helium ratios of **a** 0.0/1.0, **b** 0.05/0.95, **c** 0.1/0.9, **d** 0.2/0.8, **e** 0.3/0.7, and **f** 0.5/0.5

distribution of Fe I spectral intensity supports the predictions of iron vapour distribution in an argon–helium arc.

5 Conclusions

This work presents a computational study of gas tungsten arc welding, including the effects of metal vapour, in argon–helium shielding gas mixtures. The computational model uses the combined diffusion coefficient method, which has been extended to include three gases [23], to treat the diffusion of each gas included in the GTA welding process. Three general cases have been treated.

The first two cases did not include metal vapour. First, calculations for an argon (90% by mass) and helium (10% by mass) mixture were performed for a 5-mm arc. The predictions show good agreement with previous numerical results, demonstrating that the model can predict gas demixing reliably. Second, calculations for a wide range of argon–helium mixtures were performed for a 3-mm arc. It was found that in all cases, demixing led to the concentration of helium near the arc axis. Increasing the argon

mole fraction to about 0.3 resulted in a decreased arc temperature, while further increases had little effect on the arc temperature.

The third case comprised calculations for a wide range of argon–helium mixtures including iron vapour for a 3-mm arc. The presence of metal vapour in the arc largely determined the arc shape, arc temperature, radiative emission, and the weld pool dimensions, regardless of the argon–helium mixture used. For the very low argon mole fraction of 0.01, iron vapour was predicted to be present above the workpiece, near the cathode and in the arc fringes. As the argon mole fraction increased, metal vapour was mainly confined near the workpiece, with a small amount reaching the cathode tip.

Spectroscopic measurements of argon–helium arcs with water-cooled copper and iron workpieces were compared with the second and third sets of modelling results. Measurements of arc appearance and Fe I and He I spectral intensities were performed and showed good agreement with the numerical predictions, in particular supporting the existence of a transition in arc properties to those characteristic of an argon arc at an argon mole fraction of 0.3.

The numerical and experimental results have shown that strong demixing effects occur in argon–helium arcs and that argon–helium ratio strongly affects the metal vapour transport in the arc. This work demonstrates the importance of treating each gas separately in models of arc welding.

Funding JX thanks the CSIRO ResearchPlus postdoctoral fellowship scheme for the financial support of this work. KT, MS, and MT acknowledge the support of a Japan Society for the Promotion of Science (JSPS) Grant-in-Aid for Research Fellow (KAKENHI: Grant Number JP20J13790).

Nomenclature B , magnetic field strength; c_p , specific heat at constant pressure; d_{nozzle} , diameter of virtual nozzle; \overline{D}_I^x , combined ordinary diffusion coefficient for gas or vapour I through J ; \overline{D}_I^E , combined electric field diffusion coefficient for gas or vapour I ; \overline{D}_I^T , combined temperature diffusion coefficient for gas or vapour I ; \overline{D}_I^P , combined pressure diffusion coefficient for gas or vapour I ; e , electronic charge; E , electric field strength; g , gravitational acceleration; h , specific enthalpy; \overline{h}_I , specific enthalpy of gas or vapour I ; j , current density; j_e , electron current density; \overline{J}_I , diffusive mass flux of gas or vapour I ; k , thermal conductivity; k_B , Boltzmann's constant; \overline{m}_I , average mass of heavy species in gas or vapour I ; n , number density of gas mixture; P , pressure; S , heat flux; S_{Fe} , source term for mass of metal vapour Fe ; $S_{vap Fe}$, source term for heat of vaporisation of metal Fe ; T , temperature; U , net radiative emission coefficient; v , velocity; \overline{x}_I , sum of the mole fractions of species of gas or vapour I ; \overline{Y}_I , sum of mass fractions of species of gas or vapour I ; σ , electrical conductivity; ρ , mass density; $\overline{\tau}$, viscous stress tensor; ϕ , electrical potential; ϕ_w , anode work function

References

- Lohse M, Trautmann M, Siewert E, Hertel M, Füssel U (2018) Predicting arc pressure in GTAW for a variety of process parameters using a coupled sheath and LTE arc model. *Weld World* 62(3): 629–635
- Baeva M, Uhrlandt D (2019) Nonequilibrium simulation analysis of the power dissipation and the pressure produced by TIG welding arcs. *Weld World* 63(2):377–387
- Murphy AB, Tanaka M, Yamamoto K, Tashiro S, Satoh T, Lowke JJ (2009) Modelling of thermal plasmas for arc welding: the role of shielding gas properties and of metal vapour. *J Phys D Appl Phys* 42(19):194006
- Murphy AB (1997) Demixing in free-burning arcs. *Phys Rev E* 55(6):7473–7494
- Murphy AB, Tanaka M, Tashiro S, Sato T, Lowke JJ (2009) A computational investigation of the effectiveness of different shielding gas mixtures for arc welding. *J Phys D Appl Phys* 42(11):115205
- Tanaka M, Tashiro S, Satoh T, Murphy AB, Lowke JJ (2008) Influence of shielding gas composition on arc properties in TIG welding. *Sci Technol Weld Join* 13(3):225–231
- Lowke JJ, Morrow R, Haidar J, Murphy AB (1997) Prediction of gas tungsten arc welding properties in mixtures of argon and hydrogen. *IEEE Trans Plasma Sci* 25(5):925–930
- Tusek J (2000) Experimental investigation of gas tungsten arc welding and comparison with theoretical predictions. *IEEE Trans Plasma Sci* 28(5):1688–1693
- Marya M, Edwards GR, Liu S (2004) An investigation of the effects of gases in GTA welding of a wrought AZ80 magnesium alloy. *Weld J* 83(7):203S–212S
- Lu S, Fujii H, Nogi K (2004) Marangoni convection and weld shape variations in Ar–O₂ and Ar–CO₂ shielded GTA welding. *Mater Sci Eng A* 380(1):290–297
- Valiente Bermejo MA, Karlsson L, Svensson LE, Hurtig K, Rasmuson H, Frodigh M, Bengtsson P (2015) Effect of shielding gas on welding performance and properties of duplex and superduplex stainless steel welds. *Weld World* 59(2):239–249
- Murphy AB (1997) Transport coefficients of helium and argon–helium plasmas. *IEEE Trans Plasma Sci* 25(5):809–814
- Murphy AB (1998) Cataphoresis in electric arcs. *J Phys D Appl Phys* 31(23):3383–3390
- Murphy AB (2013) Influence of metal vapour on arc temperatures in gas–metal arc welding: convection versus radiation. *J Phys D Appl Phys* 46(22):224004
- Park H, Trautmann M, Tanaka K, Tanaka M, Murphy AB (2018) A computational model of gas tungsten arc welding of stainless steel: the importance of considering the different metal vapours simultaneously. *J Phys D Appl Phys* 51(39):395202
- Xiang J, Chen FF, Park H, Tanaka K, Shigeta M, Tanaka M, Murphy AB (2020) Numerical study of the metal vapour transport in tungsten inert-gas welding in argon for stainless steel. *Appl Math Model* 79:713–728
- Tanaka K, Shigeta M, Tanaka M, Murphy AB (2019) Investigation of the bilayer region of metal vapor in a helium tungsten inert gas arc plasma on stainless steel by imaging spectroscopy. *J Phys D Appl Phys* 52(35):354003
- Chen FF, Xiang J, Thomas DG, Murphy AB (2020) Model-based parameter optimization for arc welding process simulation. *Appl Math Model* 81(1):386–400
- Hertel M, Trautmann M, Jäckel S, Füssel U (2017) The role of metal vapour in gas metal arc welding and methods of combined experimental and numerical process analysis. *Plasma Chem Plasma Process* 37(3):531–547
- Schnick M, Fuessel U, Hertel M, Rose S, Haessler M, Spille-Kohoff A, Murphy AB (2011) Numerical investigations of the influence of metal vapour in GMA welding. *Weld World* 55(11–12): 114–120
- Lowke JJ, Tanaka M, Murphy AB (2010) Metal vapour in MIG arcs can cause (1) minima in central arc temperatures and (2) increased arc voltages. *Weld World* 54(9–10):R292–R297
- Wagner R, Siewert E, Schein J, Hussary N, Jäckel S (2018) Shielding gas influence on emissions in arc welding. *Weld World* 62(3):647–652
- Zhang XN, Murphy AB, Li HP, Xia WD (2014) Combined diffusion coefficients for a mixture of three ionized gases. *Plasma Sources Sci Technol* 23(6):065044
- Murphy AB (2001) Thermal plasmas in gas mixtures. *J Phys D Appl Phys* 34(20):R151–R173
- Fudolig AM, Nogami H, Yagi J (1996) Modeling of the flow, temperature and concentration fields in an arc plasma reactor with argon–nitrogen atmosphere. *ISIJ Int* 36(9):1222–1228
- Chen X, Sugawara M, Kikukawa N (1998) Modelling of the heat transfer and fluid flow in a radio-frequency plasma torch with argon–hydrogen as the working gas. *J Phys D Appl Phys* 31(10): 1187–1196
- Schnick M, Fussel U, Hertel M, Spille-Kohoff A, Murphy AB (2010) Metal vapour causes a central minimum in arc temperature in gas–metal arc welding through increased radiative emission. *J Phys D Appl Phys* 43(2):022001
- Yang F, Rong M, Wu Y, Murphy AB, Pei J, Wang L, Liu Z, Liu Y (2010) Numerical analysis of the influence of splitter-plate erosion on an air arc in the quenching chamber of a low-voltage circuit breaker. *J Phys D Appl Phys* 43(43):434011

29. Gomes A, Aubretton A, Gonzalez JJ, Vacquie S (2004) Experimental and theoretical study of the expansion of a metallic vapour plasma produced by laser. *J Phys D Appl Phys* 37(5):689–696
30. Murphy AB (2014) Calculation and application of combined diffusion coefficients in thermal plasmas. *Sci Rep* 4:4304
31. Lowke JJ, Morrow R, Haidar J (1997) A simplified unified theory of arcs and their electrodes. *J Phys D Appl Phys* 30(14):2033–2042
32. Lowke JJ, Tanaka M (2006) LTE-diffusion approximation for arc calculations. *J Phys D Appl Phys* 39(16):3634–3643
33. Murphy AB (2010) The effects of metal vapour in arc welding. *J Phys D Appl Phys* 43(43):434001
34. Cram LE (1985) Statistical evaluation of radiative power losses from thermal plasmas due to spectral lines. *J Phys D Appl Phys* 18(3):401–411
35. Cressault Y, Rouffet ME, Gleizes A, Meillot E (2010) Net emission of Ar-H₂-He thermal plasmas at atmospheric pressure. *J Phys D Appl Phys* 43(33):335204
36. Menart J, Malik S (2002) Net emission coefficients for argon–iron thermal plasmas. *J Phys D Appl Phys* 35(9):867–874
37. Murphy AB (1993) Diffusion in equilibrium mixtures of ionized gases. *Phys Rev E* 48(5):3594–3603
38. Xiang J, Park H, Tanaka K, Shigeta M, Tanaka M, Murphy AB (2019) Numerical study of the effects and transport mechanisms of iron vapour in tungsten inert-gas welding in argon. *J Phys D Appl Phys* 53(4):044004
39. Park H, Trautmann M, Tanaka M, Tanaka K, Murphy AB (2017) Mixing of multiple metal vapours into an arc plasma in gas tungsten arc welding of stainless steel. *J Phys D Appl Phys* 50(43):43LT03
40. Tanaka K, Shigeta M, Tanaka M, Murphy AB (2020) Investigation of transient metal vapour transport processes in helium arc welding by imaging spectroscopy. *J Phys D Appl Phys* 63(42):425202

Publisher's note Springer Nature remains neutral with regard to jurisdictional claims in published maps and institutional affiliations.